**Reentrant Spin-Glass and Large Coercive Field Observed in the Spin Integer Dimerized Honeycomb Lattice**

*Yuan-Qi Zhai, Yi-Fei Deng, Peng-Bo Jin, Zhendong Fu*, Erxi Feng, Yixi Su, Takuya Shiga, Hiroki Oshio, and Yan-Zhen Zheng**

Y.-Q. Zhai, Dr. Y.-F. Deng, P.-B. Jin, Prof. Dr. Y.-Z. Zheng,
Frontier Institute of Science and Technology (FIST), Xi'an Jiaotong University Shenzhen Research Academy, State Key Laboratory for Mechanical Behavior of Materials, MOE Key Laboratory for Nonequilibrium Synthesis of Condensed Matter,
Xi'an Jiaotong University,
99 Yanxiang Road, Xi'an, Shaanxi 710054, China
E-mail: zheng.yanzhen@xjtu.edu.cn

Prof. Dr. Z.-D. Fu,
Neutron Platform, Songshan Lake Materials Laboratory,
Dongguan 523000, China
E-mail: zdfu@pku.edu.cn

Dr. E.-X. Feng, Dr. Y.-X. Su,
Forschungszentrum Jülich GmbH, JCNS at MLZ, Lichtenbergstraße 1,
D-85747 Garching b. München, Germany

Dr. T. Shiga, Prof. Dr. H. Oshio
Graduate School of Pure and Applied Sciences,
University of Tsukuba,
Tennodai 1-1-1, Tsukuba 305-8571, Japan

Prof. Dr. H. Oshio
State Key Laboratory of Fine Chemicals
Dalian University of Technology
2 Linggong Rd., Dalian 116024, China

**Keywords**: 2D frustrated magnets, dimerized honeycomb lattice, iron(II), spin glass, neutron scattering

**Abstract**: Two-dimensional (2D) magnetic material with dimerized honeycomb lattice can be treated as a mixed-spin square lattice where quantum phase transition may occur to realize the exotic Bose-Einstein condensation of magnons at reachable experimental conditions. However, this was not successed in previously reported cases with half-integer spin centers. Herein we realize a spin integer ($S = 2$) dimerized honeycomb lattice in an iron(II)-azido compound $[Fe(4\text{-etpy})_2(N_3)_2]_n$ (FEN, 4-etpy = 4-ethylpyridine). Morphology characterization by TEM, SEM and AFM spectroscopies shows the thinnest place of the sample is ca. 13 nm, which equals to ten layers of the compound. In contrast to the common LRMO behavior magnetic, Mössbauer and polarized neutron scattering spectroscopy studies reveal that FEN exhibits a reentrant spin-glass behavior owing to the competing ferro- and antiferro-magnetic exchange-coupling interactions within the lattice. The two spin glass phases with disparate canting angles are characterized at 39 K and 28 K, respectively. By using the Curély's model we are able to simulate the two exchange-coupling constants ($J_1$ = +35.8 $cm^{-1}$ and $J_2$ = -3.7 $cm^{-1}$). This predicts a Curie temperature of 53.9 K by mean field approximation. Moreover, a very large coercive field of ca. 1.9 Tesla is observed for FEN at 2 K, making it a "very hard" van der Waals 2D magnetic material.

## 1. Introduction

Since the isolation of graphene in 2004,[1, 2] developments in two-dimensional (2D) materials have arisen on many fronts and have seen the emergence of numerous properties associated with electron mobility, mechanical strain and optical properties.[3-7] In contrast, the realization of 2D magnetism remains challenging although it has long been investigated in theory.[8] Experimentally, only a few examples approach this goal thus far, such as $CrI_3$[4], $MoS_2$[9], $FePS_3$[10], $[CrCl_2(pyrazine)_2]$[11], $[Fe(bimCl)_3]$[12], $Cr_2Ge_2Te_6$[13], $VSe_2$[14] and $MnSe_2$[15]. The main obstacle lies at the readily induced 3D long-range magnetic ordering (LRMO) between the layers by either exchange-coupling interaction through chemical bonds or dipole-dipole interaction through space. [16-18]

On the other hand, the design of specific topology in 2D material with spin frustrated feature is also fundamentally interesting. There are eleven Archimedean 2D lattices which are conceived to show quantum fluctuation down to zero Kelvin due to the antiferromagnetically coupled spins.[19] Many spin-frustrated lattices are based on the hexagons by further sharing triangles to form the famous Kagomé lattice or other hexgons to form the honeycomb lattice. In theory, the honeycomb lattice has been studied using the spin-1/2 Heisenberg antiferromagnetic model, all predicting that the ground state is a semi-classical Néel-ordered state but with small magnetic fluctuation.[20-23] For real compounds , such as $BaM_2(XO_4)_2$ (M = Co, Ni; X = P, As),[24] the quantum fluctuation is however, observed. More exotic behavior, such as 'cooperative paramagnetism' in $\lambda$-$MnO_2$ where the spins freeze with respect to dynamics is also reported.[25-27] The latter is actually in accordance with the fact that the coordination number $z = 3$ in honeycomb lattice is the smallest in 2D coordination number, which makes it possible to have larger degree of quantum fluctuations.[28]

It is however very challenging to prepare compounds with ideal honeycomb lattice. Many reported compounds show distortions.[29-32] One of the noticable distortions is the unequal distance within the lattice, which makes two edges of the haxagon shortened. Such a lattice can be called as a dimerized honeycomb lattice.[33, 34] If the dimerized spins are treated as one larger spin state this can also lead to a square lattice with mixed spins and provide a model system for studying quantum phase transitions. [35, 36] In particular, a famous magnetic insulator $TlCuCl_3$ with $Cu^{2+}$ dimers forming square lattice is shown to realize Bose-Einstein condensation of magnons.[36, 37] However, for dimerized honeycomb lattice, there are only two reported cases with half-integer spin centers,[29-32] and no integer spin centers are studied. One of the reasons is that in the preparation of the interger spin dimerized honeycomb lattice, especially for spin-2, air-sensitive metal ions, such as iron(II), are required.

We show here that the 4-ethylpyridine (4-etpy) ligand can overcome this difficulty when reacting with iron(II) and azide salts. Its pyridyl part bearing a pair of lone electron can coordinate to the in-plane metal ions, while its aliphatic ethyl chain is compartible with organic solvents and can separate the layers with only van der Waals forces. Such a sandwich type structure is also protective for air-sentitive metal ions. The formed material is formulated as $[Fe(4\text{-etpy})_2(N_3)_2]_n$ (FEN), which features a dimerized spin-2 honeycomb lattice due to the alternating 1,1-end-on (EO) and 1,3-end-to-end (EE) azido bridges and exhibits disparate magnetic behavior compared to its odd spin counterparts. Magnetic, Mössbauer and polarized neutron scattering spectroscopy studies reveal that below 39 K FEN displays the reentrant spin glass transition due to the reorientation of the canted spins. Moreover, a large coercive field of ca. 1.9 Tesla is recorded at 2 K, which makes FEN a "very hard" 2D van der Waals magnet.

**2. Results and discussion**

**2.1. Crystallography down to 20 K**

X-ray crystallographic data measured at 150 K and 20 K reveal that FEN crystallizes in the monoclinic space group $P2_1/c$ (**Figure 1**, Figure S1 and Table S1). Each Fe(II) site is situated in a pseudoctahedral coordination environment with Fe-N bond distances of ~ 2.2 Å (Table S2), consistent with the high spin Fe(II) ions. The azido bridges exhibit two coordination modes: i) EO mode in the centrosymmetric [$Fe_2$] unit, ii) EE mode between the [$Fe_2$] units; thus forming a neutral 2D layer. The dimerized Fe-Fe distance is 3.462(3) Å, while the averaged Fe-Fe distance between the dimers is 6.040(3) Å. The two EE azido bridges are not centrosymmetric-related, and the dihedral angle between two neighboring [$Fe_2$] units is 83.25(8)°. The minimum interlayer Fe-Fe distance is 13.2 Å, indicating the thickness of a single layer of FEN is ca. 1.3 nm. No interlayer π-π stacking interactions or hydrogen bonds are found, indicating that the layers are stacked by van der Waals force only. To further investigate the temperature-dependent structural transitions we determined the X-ray single-crystal structure down to 20 K and found similar crystallopraphic parameters (Table S1 and S2), which indicates that the structure of FEN remains unchanged down to 20 K.

**2.1. Layered morphology**

Scanning electron microscope (SEM) and transmission electron microscopy (TEM) were used to investigate the morphology of the FEN sample. A close-up view on the powder samples with SEM study evidences the layered structure of FEN as the stacking of multiple layers (**Figure 2**a and 2b), the purity of which was confirmed by powder X-ray diffraction (Figure. S2). However, the observation of clear edges of layers is hard for the highly aggregated powder samples. Thus we disperse the sample with methanol, and dropped it onto a silicon nitride membrane for high resolution TEM measurement. Figure 2c shows well-defined irregular

layers, which is consistent with the SEM analysis. Zooming in these layers (Figure 2d-2f) gives a typical size of ca. 40 nm for the width of the edges.

However, the thickness of such layer is unknown. Hence, atomic force microscopy (AFM) was used to determine the thickness of these flakes (**Figure 3**). By spinning the diluted methanol solution of these flakes an ultra- thin and flat film of FEN is deposited onto a silicon wafer substrate. The topological and height analyses for AFM images show the thinnest place of the is about 13 nm, which amounts to ca. ten layers of FEN sheets as the thickness of a single-layer of FEN was determined to be 1.3 nm.

**2.2. Magnetic properties**

Dc magnetic susceptibility measurements for FEN are conducted within the temperature range of 2–300 K under various fields (**Figure 4**a and S3). The effective magnetic moment ($u_{\text{eff}}$) is 5.45 $\mu_B$ at 300 K, consistent with the high spin state ($S$ = 2) for the Fe(II) ion with substantial orbital contribution. Upon cooling, the $\chi T$ product decreases gradually before up rising sharply up to 28 K. There is a "shoulder" appears at 39 K, indicating a phase transition. In the structure of FEN, there are no inversion centres between the dimers linked by single EE-$N_3$ ligands, compatible with the onset of spin canting by Dzyaloshinskii-Moriya (DM) interaction.[38-39] In addition, the magnetic anisotropy of single Fe(II) ions also contribute to the spin-canting behaviour.[40-41] *Ab initio* calculations show a large positive $D$ value (14.3 $cm^{-1}$) and a well-separated $g$-tensers ($g_x$ = 1.98, $g_y$ = 2.36, $g_z$ = 2.53), indicating the magnetic anisotropy is of easy-plane type. By analysing the d-orbital diagram (Figure S10), we can see the anisotropic axis of the Fe(II) ion is pointing directly to one of the EE mode azido bridges.

There are two different in-plane magnetic interactions, denoted as $J_1$ and $J_2$ (see Figure 4a), namely representing the couplings within and between the [$Fe_2$] units. This forms a dimerized

spin-2 honeycomb lattice, which can be fitted by the Curély's model[42] based on the following Hamiltonian,

$$H = -J_1 \sum_{i,j(odd)} S_{i,j} S_{i+1,j} - J_2 \sum_{i,j} S_{i,j} S_{i,j+1} \quad (1)$$

which gives the susceptibility as:

$$\chi = \frac{1}{6k_B T} \frac{(g_1{}^2 + g_2{}^2) w_1 + 2 g_1 g_2 w_2}{(1-u^2 v^2)(1-v^2)} \quad (2)$$

where $w_1 = (1+uv)^2(1+v^2)$ ; $w_2 = 2v(1+uv)^2 + u(1-v^2)^2$ ; $g_1$ and $g_2$ are Landé factors; $k_B$ is the Boltzmann constant; $u$ and $v$ are Langevin functions and the coupling constants ($J_1$ and $J_2$) are multiplied by a normalization factor $S(S+1)$ in a classical way.[43] The best fit for the data in the temperature range of 40 to 300 K yields $J_1$ = +35.8 cm$^{-1}$, $J_2$ = -3.7 cm$^{-1}$ and $g_1$ = $g_2$ = 2.36 with $R = 6.2\times10^{-6}$, where $R = \Sigma(\chi_{obs}-\chi_{calc})^2 / \Sigma(\chi_{obs})^2$. The obtained $J$ values indicate alternating ferromagnetic and antiferromagnetic couplings within the lattice.[44]

To characterize the low-temperature abrupt rise in the temperature-dependent susceptibility data, the field-cooled (FC) and zero-field-cooled (ZFC) magnetization measurements are performed under different fields (Figure 4b). At all the fields measured, the FC magnetization increases rapidly below 39 K and rises to a peak point at about 28 K. This is consistent with the previous $\chi T$ vs. $T$ plot.

Both in-phase ($\chi'$) and out-of-phase ($\chi''$) components of the ac susceptibility data exhibit sharp and frequency-dependent maxima at about 39 K. There is another frequency-dependent

peak for $\chi'(T)$ appearing at around 28 K, followed by a broad, frequency dependent hump (see the inset of **Figure 5**a) at about 25 K. The $\chi''(T)$ shows only frequency dependent humps at about 25 K, but no peaks at about 28 K. As the applied ac frequency increases, the hump at around 25 K shifts to higher temperatures, which is often taken as a sign of either a spin glass or a superparamagnetic behavior. A convenient way to understand the nature of the spin-glass-freezing process lies in the examination of relative shift *K* of the peak temperature per decade frequency using the following expression,

$$K = \frac{\Delta T_f}{T_f \Delta \log_{10}(f)} \tag{3}$$

where $T_f$ is the freezing temperature and $f$ is the driving frequency. Experimentally $T_f$ is commonly determined from the maximum of $\chi'$, while in this case the inflection point of $\chi''$ is used because the hump at around 25 K in $\chi'(T)$ is not clear. Both methods have been widely used to extract $T_f$ in spin glass systems and give comparable results in dynamic scaling analysis.[47] The calculated *K* value of 0.01 is in good agreement with the reported values for canonical spin glasses, precluding the superparamagnetic category.[48]

Another characteristic of spin glasses is the dynamical slowing down of the spin fluctuations on approaching the spin glass transition temperature $T_g$ from above. The maximum relaxation time $\tau_m$ and $T_f$ obeys the following power-law relation,[48]

$$\tau_m = \tau_0 \left(\frac{T_f}{T_g} - 1\right)^{-zv} \tag{4}$$

where $\tau_m = (2\pi f)^{-1}$, $\tau_0$ is the relaxation time of individual particle magnetic moment, $z$ is dynamic critical exponent, and $v$ is the critical exponent of the correlation length $\xi = (T_f/T_g - 1)^{-v}$. Eq. (3) can be rewritten as

$$\log_{10}\tau_m = \log_{10}\tau_0 - zv\log_{10}(\frac{T_f}{T_g} - 1) \quad (5)$$

The least-square fit of the data by Equation (4) yields a spin-glass transition temperature $T_g$ = 22.2(1.0) K. In the inset of Figure 5a, we plot $\log_{10}(\tau_m)$ versus $\log_{10}(T_f/T_g - 1)$, which shows a linear behavior. The straight line fit gives $\tau_0 = 10^{-11.4(3)}$ s and $zv$ = 9.2(3). The value of relaxation time $\tau_0 = 10^{-11.4(3)}$ s locates in the characteristic range, $10^{-10}$-$10^{-13}$ s, usually derived for canonical spin glass. The value of $zv$ holds good in the range between 4 and 12 found in the spin glass materials.[48-50] Therefore the dynamical scaling parameters are in accordance with spin glass state formation at low temperatures for FEN.

Magnetic bistability is observed in all magnetization versus field scans below 40 K (Figure 5b, S5 and S6). FEN behaves like a "hard magnet" with a large coercive field of 1.9 T at 2 K. This coercive field of FEN is much larger compared to 2D magnets,[12-18] indicating the potential interactions between the layers.

Field-dependent isothermal magnetizations at 39 K and 28 K increase slowly and linearly at high field region, and the values of 0.88 and 0.99 $\mu_B$ at 7 T are far from saturation (Figure S4). These features are consistent with the spin canting behavior. Taking the two ferromagnetically coupled Fe(II) ions as one node (as verified with polarized neutron scattering method in the next section), the canting angles for FEN at 39 K and 28 K are estimated to be 2.8° and 6.2°, respectively. As shown in **Figure 6**, we propose the spin canting topology maps at 39 K (a) and

28 K (b). At high temperatures up to at least 100 K, the nearest Fe(II) moments are ferromagnetically coupled, while the intra-layer orientations of the ferromagnetic spin pairs are random. Upon cooling, the first spin canting phase appears at $T$ = 39 K owing to the magnetic anisotropy. All the in-plane spins are orientated with respect to the topology of the ferromagnetic interactions in one direction and the antiferromagnetic interactions in the other. When the temperature is further lowed, the spin re-orientation occurs, leading to a more stable canting angle below 28 K. As also obtained from *ab initio* calculations, the direction of the ground state magnetic moment on each Fe(II) site is equal to this most stable spin canting angle, confirming the stabilizing of such spin orientations at low temperature.

### 2.3. $^{57}$Fe Mössbauer spectroscopy

FEN was characterized by $^{57}$Fe Mössbauer spectroscopy[51] between 14 and 45 K. The spectra of the whole temperature range can be fitted with doublets (above 30 K) and sextets (below 25 K), see the solid lines in **Figure 7** and the corresponding parameters in Table S3. At 45 K, the spectrum consists of a quadrupole doublet broadened by paramagnetic relaxation and characterized by an isomer shift of $\delta$ = 1.198 mm·s$^{-1}$, a quadrupole splitting of $\Delta E_Q = 2.695$ mm·s$^{-1}$, which is consistent with the high spin Fe(II) centers[52]. In the whole temperature range of measurement, the doublets are well developed above 30 K while the presence of closely connected asymmetric sextets occur upon cooling below 25 K, which may indicate the long- or short magnetic ordering or slow relaxation on Mössbauer timescale.[52]

### 2.4. Polarized Neutron Scattering Analyses

In order to further investigate the nature of magnetism in FEN from a microscopic point of view, we performed diffuse neutron scattering with polarization analysis. In the *xyz*-polarization analysis, the spin-flip (SF) and non-spin-flip (NSF) differential cross sections are

measured for an *xyz*-polarized incident beam, giving a total of six partial cross sections, labeled $d\sigma_{SF}^{(x,y,z)} / d\Omega$ and $d\sigma_{NSF}^{(x,y,z)} / d\Omega$. The differential magnetic cross section can be extracted from either

$$\frac{d\sigma_{Mag}}{d\Omega} = 2\left(\frac{d\sigma_{SF}^{x}}{d\Omega} + \frac{d\sigma_{SF}^{y}}{d\Omega} - 2\frac{d\sigma_{SF}^{z}}{d\Omega}\right) \quad (6)$$

or

$$\frac{d\sigma_{Mag}}{d\Omega} = 2\left(2\frac{d\sigma_{NSF}^{z}}{d\Omega} - \frac{d\sigma_{NSF}^{x}}{d\Omega} - \frac{d\sigma_{NSF}^{y}}{d\Omega}\right) \quad (7)$$

These two expressions correspond to independent measurements, and the magnetic differential cross section is taken as their average to reduce systematic errors.[53]

When a polarized neutron beam passes through an unsaturated ferro/ferri-magnetic material, the state of polarization *P* is changed due to the Larmor precession of the neutron spins in the magnetic field of magnetic domains. The reduction of *P* of a polarized neutron beam after transmission through a magnetic material is known as neutron depolarization. The polarization *P* can be expressed as

$$P = \frac{I_{NSF} - I_{SF}}{I_{NSF} + I_{SF}} = \frac{R-1}{R+1} \quad (8)$$

where $I_{NSF}$ and $I_{SF}$ are the diffracted intensities measured with the neutron flipper turned off (NSF) and on (SF), respectively. $R = I_{NSF}/I_{SF}$ is called the flipping ratio and is a measurable parameter in a neutron scattering experiment. It is obvious that neutron depolarization will cause a decrease in $R$. Experimentally, we determined the flipping ratio $R$ by measuring the count rates $I_{NSF}$ and $I_{SF}$ at the peak of the strongest Bragg reflection (100) at $Q = 0.49$ Å$^{-1}$. The flipping ratio was measured from 4 to 58 K, in both zero-field-cooled (ZFC) and field-cooled (FC) protocols. The temperature dependence of the flipping ratio is plotted in Figure 4b. The flipping ratio is constant above 40 K, suggesting that no neutron depolarization occurred due to the absence of ferro/ferri-magnetic contribution. When the temperature decreases from 40 K, two drops, especially in the FC curve, can be seen at 39 K and 28 K. As shown in Figure 4b, these drops in the flipping ratio correspond to the sharp changes observed in the magnetic susceptibility and mark the onset of the in-plane ferromagnetic contributions. The flipping ratio decreases gradually on cooling from 39 to 28 K, suggesting that the in-plane spin reorientation happens gradually, not suddenly. Below 28 K the flipping ratio falls rapidly to about 2.4 in the ZFC curve. This means the incident neutron spins are only partially depolarized, precluding the emergence of macroscopic ferromagnetic domains. Therefore the temperature dependence of the flipping ratio suggests that, the in-plane ferromagnetic contribution (spin canting) results in the steep decrease of the flipping ratio at 39 and 28 K, respectively.

The measurement with *xyz*-polarization method on DNS was performed at 3.3, 43 and 100 K. The total neutron scattering intensity before separation is shown as a function of $Q$ in **Figure 8**. The scattering profiles and intensities measured at different temperatures are nearly identical. The difference profile obtained by subtracting the scattering intensity for 43 K from the one for

3.3 K is depicted in Figure S7, from which we can conclude that the peaks located at 28 and 39 K in ac susceptibility can be attributed to the in-plane spin canting and re-orientation in FEN. In order to further verify this point, the temperature-dependence of the peak intensity of the strongest Bragg reflection (110) was measured and plotted in Figure S8. The slow decrease of the peak intensity with increasing temperature is due to the increasing thermal vibrational amplitude of atoms, namely a normal Debye-Waller behavior. There is no sharp increase when the temperature crosses 28 and 39 K from above, in accordance with the spin glass behavior.

The magnetic neutron scattering intensities for 43 and 100 K were extracted by means of polarization analysis, as shown in Figure S9. The signal is noisy because the background of the spin-incoherent scattering from hydrogen atoms is high. But the upturn at low $Q$ is obvious, indicative of ferromagnetic short-range correlations. The analysis of the spin correlations starts with the differential magnetic scattering cross section of spin pairs, which is powder-averaged and can be expressed as [54-55]

$$\frac{\mathrm{d}\sigma_{\mathrm{mag}}}{\mathrm{d}\Omega} = \frac{2}{3}S(S+1)\left(\frac{\gamma e^2}{mc^2}\right)^2 f^2(Q)$$

$$+\left(\frac{\gamma e^2}{mc^2}\right)^2 f^2(Q)\sum_n\left[a_n\frac{sinQr_n}{Qr_n} + b_n\left(\frac{sinQr_n}{Q^3r^3{}_n} - \frac{cosQr_n}{Q^2r^2{}_n}\right)\right] \qquad (9)$$

where $(\gamma e^2/mc^2) = -0.54\times10^{-12}$ cm is the magnetic scattering length, $S = 2$ is the spin quantum number of $Fe^{2+}$ ions, $f(Q)$ is the magnetic scattering form factor, $r_n$ is the distance between two magnetic ions, and $a_n$ and $b_n$ are related to the probability of finding spin pairs with parallel components and are given by [55]

$$a_n = S(S+1)sin^2\theta$$

$$b_n = S(S+1)(2cos^2\theta - sin^2\theta) \quad (10)$$

$\theta$ is the azimuth angle between the directions of magnetic moments and their connecting line. As mentioned in the analysis of the dc susceptibility data, the intra-dimer magnetic interaction is ferromagnetic and is much stronger than the inter-dimer one. Hence the calculation of short-range spin correlations is carried out for a single dimer with two spins in parallel. $a_n$ and $b_n$ are integrated over the azimuth angle $\theta$ from 0 to $2\pi$ to cover the in-plane rotation of the spin dimer. The calculated spin correlations of the $Fe^{2+}$ spin dimers in FEN is shown as the blue line in Figure S9, in agreement with the experimental data measured at 43 and 100 K. Therefore the magnetic scattering intensities can be explained by the ferromagnetic spin dimers in FEN. It can also be learned that the intra-dimer coupling is quite strong since the short-range spin correlations still exist at 100 K.

From the above analysis with magnetic susceptibility and polarized neutron scattering methods, the emergence of significant ferromagnetic contribution at 39 and 28 K is believed to originate from the collective in-plane canting of Fe(II) spin pairs. Upon further cooling below 28 K, FEN shows a spin-glass behavior, whose dynamic scaling parameters are in agreement with those of canonical spin glasses. However, taking in account of the partial magnetic order at 28 and 39 K, we attribute this spin-glass behavior to a reentrant spin-glass-like (RSG-like) transition owing to the freezing of spin components transverse to the mean magnetization.[56] Such reentrance behavior has been found in many magnetic systems with a strong

ferromagnetic nearest-neighbor coupling and a weaker antiferromagnetic next-nearest-neighbor coupling.[57] Our polarized neutron scattering study on FEN clearly shows that a RSG-like phase may co-exist with magnetic orders as what has often been reported.[58-59]

### 2.6. Electronic Band Structures and Estimation of Curie temperature

We further investigate the electronic properties of FEN using first-principles calculations with the CASTEP program integrated in the Materials Studio platform. First, the X-ray crystal structure was fully optimized, which does not change lattice parameters, bond lengths and angles of FEN much. Figure S11 displays our calculated energy band structures and partial density of states (PDOS) for FEN. It is clear that the monolayer of FEN shows semiconducting properties with a narrow band gap of 0.412 eV. Since the bridges between Fe(II) sites are all $N^{3-}$ ligands, a strong orbital overlap between Fe and N can be estimated, indicating the effective charge transfer through the Fe−N bonds. The calculated Curie temperature ($T_c$) by using mean field approximation is 53.9 K, which is a bit higher than our experimental result due to the lack of considering the magnetic anisotropy from Fe(II) ions. This equals to 2/3 energy gap between the ground and the first excited state, which is the energy changing by magnetic moment reversal of one Fe(II) site.[60-62]

## 3. Conclusion

In summary, we realized a dimerized honeycomb lattice with integer spins ($S$ = 2) in a compound FEN by using the metal-organic synthetic approach. TEM, SEM and AFM analyses show the mophology of the sample is also layered and the thinnest place comprises only ten layers. Magnetic, Mössbauer and polarized neutron scattering spectroscopy studies reveal an reentrant spin glass behavior with two spin canting phases occurring at $T$ = 39 and $T$ = 28 K, owing to the competing intra-layer ferro- and antiferro-magnetic exchange-coupling

interactions. Morevoer, a large coercive field of ca. 1.9 Tesla is recorded at 2 K, which makes FEN a "very hard" van der Waals magnet. As 2D topologically-frustrated magnets largely remain unexplored in addition to optimise the geometry by chemical means future work will endeavor to reduce the number of material layers. By doing so, the authentic 2D property of the magnetic material may be revealed.

## 4. Experimental Section/Methods

*Materials.* All chemicals were commercially available and were used as received. All the solvents were dehydrated and deoxygenated by Solvent Purification Systems prior to use. All manipulations were performed under a dry and oxygen-free argon atmosphere by using Schlenk techniques or in a glovebox. Caution: Although no such behavior was observed during the present work, azido salts are potentially explosive and should be handled with care.

*Preparation of* $[Fe(4\text{-etpy})_2(N_3)_2]_n$. Compound was prepared under an insert $Ar_2$ atmosphere by the subcomponent reaction of $FeCl_2$, 4-Ethylpyridine and $NaN_3$ in methanol. 4-Ethylpyridine (108 mg, 1 mmol) was added to a methanolic solution containing anhydrous $FeCl_2$ (63 mg, 0.5 mmol) and $NaN_3$ (65 mg, 1 mmol). The reaction was carried out under continuous stirring for 6 h at room temperature followed by filtering through Celite. Yellow plate crystals suitable for X-ray diffraction were obtained by cooling the filtrate at 0 °C (76 mg, ca. 43 % yield, based on Fe).

*X-Ray crystallography data.* Crystal data of FEN at 150 K were collected on a Bruker Apex CCD area-detector diffractometer using Mo Kα (λ = 0.71073 Å) radiation. Absorption corrections were applied using the multi-scan program SADABS.[63] The structures were solved using direct methods and refined with a full-matrix least-squares technique using SHELXTL programpackage.[64] Anisotropic thermal parameters were assigned to all non-hydrogen atoms.

The hydrogen atoms were generated geometrically. Data collection and structural refinement parameters are given in Table S1 and selected bond distances and angles are given in Table S2. Crystal data of FEN at 20 K were collected at High Energy Accelerator Research Organization (KEK) in Japan. The alert PLAT029_ALERT_3_A mentioned in checkcif_20K.pdf is due to the experiments using the KEK synchrotron. The detector is cylindrical and therefore has a huge diffraction angle range but can only rotate the crystal along one axis. Therefore all possible reflections cannot be obtained. CCDC-1418339 contains the crystallographic data that can be obtained via www.ccdc.cam.ac.uk/conts/retrieving.html (or from the Cambridge Crystallographic Data Centre, 12, Union Road, Cambridge CB21EZ, UK; fax: (+44) 1223-336-033; or deposit@ccdc.cam.ac.uk). The Powder X-ray diffraction (PXRD) measurements were recorded on a Rigaku Smartlab X-ray diffractometer and the experimental patterns matched the simulated one well, confirming the purity of the sample.

*Morphology charaterizations.* SEM analysis was carried out on gold sprayed powder samples using a HITACHI SU6600 field-emission scanning electron microscope with an accelerating voltage of 5 kV. TEM analysis with solution dispersed sample was carried out on a FEG JEOL 2100F transmission electron microscope operating at 200 kV. AFM analysis was carried out on a NT-MDT Sover Next atomic force microscopy with solution dispersed sample. The solution dispersed samples for TEM and AFM measurements are prepared by dispersing a small amount of samples into methanol, then the solution was dropped onto silicon nitride membrane for TEM measurement and clean silicon wafer with spinning, forming a ultra- thin and flat layer for AFM measurement. All these operations were done inside the glovebox before the samples were transferred for either SEM, TEM or AFM measurement.

*Magnetic properties.* Magnetic susceptibility measurements on polycrystalline samples of

FEN were carried out on a Quantum Design MPMS-XL7 SQUID and MPMS-SQUIDVSM-094 magnetometer. Direct-current (dc) susceptibility measurements were performed in the temperature range 2−300 K under dc fields of 50−5000 Oe. Dc magnetization curves were measured in the temperature range 2−41 K under dc fields up to 7 T. Alternating-current (ac) susceptibility measurements were carried out at frequencies between 1 and 1500 Hz with an ac field of 3.5 Oe. Diamagnetic corrections were calculated from Pascal constants and applied to all the constituent atoms and sample holder.

*Polarized neutron scattering measurements.* Diffuse neutron scattering with polarization analysis was performed on the cold neutron time-of-flight spectrometer DNS[65] at Heinz Maier-Leibnitz Zentrum in Garching, Germany. The wavelength of the incident neutrons was 4.2 Å, allowing an accessible range of the scattering vector Q to be from 0.3 to 2.7 $Å^{-1}$. About 4 grams of powder sample were sealed in a cylindrical aluminium container under helium atmosphere and mounted in a $^4$He close-cycle cryostat. The investigated temperature range was from 3.3 to 100 K. Within the quasistatic approximation, the nuclear coherent, spin-incoherent, and magnetic scattering intensities can be separated simultaneously with the xyz-polarization method in the spin-flip (SF) and non-spin-flip (NSF) channels.[66]

*Theoretical calculations. Ab initio* calculations, using state-average Complete-Active-Space-Self-Consistent Field (SA)-CASSCF and N-electron valence perturbation theory to second order (NEVPT2), were performed using the ORCA 4.0 computational package.[67] The active space was composed of 6 metal 3d electrons and 5 3d orbitals [CAS (6, 5)], with 5 state for quintet state and 35 for triplet states, as has been used by many works.[68] The spin-orbit coupling based mean field approximation (SOMF) was used in this system. The basis sets for iron and coordinated nitrogen atoms was polarized triple-ζ-quality basis set (def2-TZVP), while

the smaller basis set (def2-SVP) was used for the other remote atoms.[69-70] Meanwhile, we also considered the scalar relativistic effects by including a standard second-order Douglas-Kroll-Hess (DKH2)[71-72] for iron (III) center and the auxiliary basis set def2/J was used in conjunction with the resolution of identity approximation. The structure of computed model is taken from a fragment of the X-ray experimental crystal structure of FEN with only one Fe(II) ion taken into account and others replaced by diamagnetic Zn(II) ion. Moreover tight SCF convergence criteria was used to maintain the calculation accuracy. The Cambridge Sequential Total Energy Package (CASTEP) program within the Materials Studio was used to calculate the electronic band structures and the densities of the states (DOSs). Before the calculation, geometric optimization was carried out until the high convergence accuracy meets. The exchange-correlation energy was calculated using Perdew-Burke-Ernzerhof (PBE) modification to the generalized gradient approximation (GGA). The convergence threshold for the self-consistent field was $1 \times 10^{-6}$ eV/atom. The Brillouin zone has been sampled with a highly converged (0.015 /Å) set of k points, using grids up to ($2 \times 2 \times 2$) points according to the Monkhorst Pack scheme.

**Supporting Information**

Supporting Information is available from the Wiley Online Library or from the author.

**Acknowledgements**

Y.-Q. Zhai and Y.-F. Deng contributed to this work equally. This work was supported by Shenzhen Science and Technology Program (JCYJ20180306170859634), Natural Science Foundation of China (Nos. 21971203, 21773130, 21620102002, 11574244, and 11875325), State Key Laboratory for Mechanical Behavior of Materials (20182006), Key Laboratory

Construction Program of Xi'an Municipal Bureau of Science and Technology (201805056ZD7CG40), the Cyrus Chung Ying Tang Foundation, the Fundamental Research Funds for the Central Universities. This work was performed under the approval of the Photon Factory Program Advisory Committee (Proposal No. 2016G175). We also thank the Instrument Analysis Center of Xi'an Jiaotong University for Dr Huang Chang's assistance with magnetic property measurement, Center for Advancing Materials Performance from the Manoscale of Xi'an Jiaotong University for Dr Peng Zhang and Dr Chaowei Guo's assistance with SEM and TEM measurements, School of Electronic Science and Engineering of Xi'an Jiaotong University for Dr Bo Jiao's assistance with AFM measurement.

Received: ((will be filled in by the editorial staff))
Revised: ((will be filled in by the editorial staff))
Published online: ((will be filled in by the editorial staff))

**References**

[1] K. S. Novoselov, A. K. Geim, S. V. Morozov, D. Jiang, Y. Zhang, S. V. Dubonos, I. V. Grigorieva, A. A. Firsov. *Science* **2004**, *306*, 666.

[2] K. S. Novoselov. *Rev. Mod. Phys*. **2011**, *83*, 837.

[3] V. Laget, C. Hornick, P. Rabu, M. Drillon, R. Ziessel. *Coord. Chem. Rev.* **1998**, *178*, 1533.

[4] B. Huang, G. Clark, E. Navarro-Moratalla, D. R. Klein, R. Cheng, K. L. Seyler, D. Zhong, E. Schmidgall, M. A. McGuire, D. H. Cobden, W. Yao, D. Xiao, P. Jarillo-Herrero, X.-D. Xu. *Nature* **2017**, *546*, 270.

[5] M. Buscema, J. O. Island, D. J. Groenendijk, S. I. Blanter, G. A. Steele, H. S. J. van der Zanta, A. Castellanos-Gomez. *Chem. Soc. Rev*. **2015**, *44*, 3691.

[6] C.-Y. Zhi, Y. Bando, C.-C. Tang, H. Kuwahara, D. Golberg. *Adv. Mater.* **2009**, *21*, 2889.

[7] M. S. Dresselhaus, G. Chen, M. Y. Tang, R.-G. Yang, H. Lee, D.-Z. Wang, Z.-F. Ren, Jean-Pierre Fleurial, P. Gogna. *Adv. Mater.* **2007**, *19*, 1043.

[8] J. M. Kosterlitz, D. J. Thouless. *J. Phys. C* **1973**, *6*, 1181.

[9] A. Castellanos-Gomez, M. Poot, G. A. Steele, H. S. J. van der Zant, N. Agraït, G. Rubio-Bollinger. *Adv. Mater.*, **2012**, *24* , 772.

[10] J.-U. Lee, S. Lee, J. H. Ryoo, S. Kang, T. Y. Kim, P. Kim, C.-H. Park, J.-G. Park, H. Cheong. *Nano Lett.* **2016**, *16*, 7433.

[11] K. S. Pedersen, P. Perlepe, M. L. Aubrey, D. N. Woodruff, S. E. Reyes-Lillo, A. Reinholdt, L. Voigt, Z.-S. Li, K. Borup, M. Rouzières, D. Samohvalov, F. Wilhelm, A. Rogalev, J. B. Neaton, J. R. Long, R. Clérac. *Nat. Chem.* **2018**, *10*, 1056.

[12] J. López-Cabrelles, S. Mañas-Valero, I. J. Vitórica-Yrezábal, P. J. Bereciartua, J. A. Rodríguez-Velamazán, J. C. Waerenborgh, B. J. C. Vieira, D. Davidovikj, P. G. Steeneken, H. S. J. van der Zant, G. Mínguez Espallargas, E. Coronado. *Nat. Chem.* **2018**, *10*, 1001.

[13] C. Gong, L. Li, Z.-L. Li, H.-W. Ji, A. Stern, Y. Xia, T. Cao, W. Bao, C.-Z. Wang, Y. Wang, Z. Q. Qiu, R. J. Cava, S. G. Louie, J. Xia, X. Zhang. *Nature* **2017**, *546*, 265.

[14] M. Bonilla, S. Kolekar, Y.-J. Ma, H. C. Diaz, V. Kalappattil, R. Das, T. Eggers, H. R. Gutierrez, M.-H. Phan, M. Batzill . *Nat. Nanotechnol*. **2018**, *13*, 289.

[15] D. J. O'Hara, T.-C. Zhu, A. H. Trout, A. S. Ahmed, Y. K. Luo, C. H. Lee, M. R. Brenner, S. Rajan, J. A. Gupta, D. W. McComb, R. K. Kawakami. *Nano Lett.* **2018**, *18*, 3125.

[16] K. S. Novoselov, A. Mishchenko, A. Carvalho, A. H. C. Neto. *Science* **2016**, *353*, aac9439.

[17] K. S. Burch, D. Mandrus, J. G. Park. *Nature* **2018**, *563*, 47.

[18] M. Gibertini, M. Koperski, A. F. Morpurgo, K. S. Novoselov. *Nat. Nanotechnol*. **2019**, *14*, 408.

[19] J. Richter, J. Schulenburg, A. Honecker. *Lect. Notes Phys.* **2004**, *645*, 85.

[20] J. Oitmaa, C. J. Hamer, Z. Weihong. *Phys. Rev. B* **1992**, *45*, 9834.

[21] Z. Weihong, J. Oitmaa, C. J. Hamer. *Phys. Rev. B* **1991**, *44*, 11689.

[22] J. B. Fouet, P. Sindzingre, C. Lhuillier. *Eur. Phys. J. B* **2001**, *20*, 241.

[23] A. Mattsson, P. Frojdh. *Phys. Rev. B* **1994**, *49*, 3997.

[24] L. P. Regnault, J. Rossat-Mignod in *Phase transitions in quasi two-dimensional planar magnets*, edited by L.J. De Jongh (Kluwer Academic Publishers, **1990**), pp. 271-320.

[25] P. W. Anderson. *Phys. Rev.* **1956**, *102*, 1008.

[26] J. E. Greedan, N. P. Raju, A. S. Wills, C. Morin, S. M. Shaw, J. N. Reimers. *Chem. Mater.* **1998**, *10*, 3058.

[27] J. E. Greedan. *J. Mater. Chem.* **2001**, *11*, 37.

[28] B. Grunbaum, G. C. Shephard: *Tilings and Patterns*, W. H. Freeman and Company, New York (**1987**).

[29] X.-Y. Wang, L. Wang, Z.-M. Wang, S. Gao. *J. Am. Chem. Soc.* **2006**, *128*, 674.

[30] X.-T. Wang, Z.-M. Wang, S. Gao. *Inorg. Chem.* **2007**, *46*, 10452.

[31] A. Escuer, J. Cano, M. A. S. Goher, Y. Journaux, F. Lloret, F. A. Mautner, R. Vicente. *Inorg. Chem.* **2000**, *39*, 4688.

[32] A. Escuer, F. A. Mautner, M. A. S. Goher, M. A. M. Abu-Youssef, R. Vicente. *Chem. Commun.* **2005**, *5*, 605.

[33] L. Fritz, R. L. Doretto, S. Wessel, S. Wenzel, S. Burdin, M. Vojta. *Phys. Rev. B.* **2011**, *83*, 174416.

[34] F.-J. Jiang. *Phys. Rev. B.* **2012**, *85*, 014414.

[35] S. Sachdev. *Nat. Phys.* **2008**, *4*, 173.

[36] T. Giamarchi, C. Ruegg, O. Tchernyshyov. *Nat. Phys.* **2008**, *4*, 198.

[37] T. Nikuni, M. Oshikawa, A. Oosawa, H. Tanaka. *Phys. Rev. Lett*. **2000**, *84*, 5868.

[38] I. Dzyaloshinsky. *Phys. Chem. Solids* **1958**, *4*, 241.

[39] T. Moriya. *Phys. Rev.* **1960**, *120*, 91.

[40] Z.-L. Huang, M. Drillon, N. Masciocchi, A. Sironi, J.-T. Zhao, P. Rabu, P. Panissod. *Chem. Mater.* **2000**, *12*, 2805.

[41] R. Feyerherm, A. Loose, P. Rabu, M. Drillon. *Solid State Sci.* **2003**, *5*, 321.

[42] J. Curély, F. Lloret, M. Julve. *Phys. Rev. B.* **1998**, *58*, 11465.

[43] I. Negodaev, C. de Graaf, R. Caballol. *J. Phys. Chem. A*. **2010**, *114*, 7553.

[44] S. Konar, E. Zangrando, M. G. B. Drew, T. Mallah, J. Ribas, N. R. Chaudhuri. *Inorg. Chem.* **2003**, *42*, 5966.

[45] L. D. Tung. *Phys. Rev. B*. **2006**, *73*, 024428.

[46] L. D. Tung, M. R. Lees, G. Balakrishnan, D. M. Paul. *Phys. Rev. B* **2007**, *75*, 104404.

[47] J. Mattsson, T. Jonsson, P. Nordblad, H. A. Katori, A. Ito. *Phys. Rev. Lett.* **1995**, *74*, 4305.

[48] J. A. Mydosh. Taylor &Francis, London, **1993**

[49] P. C. Hohenberg, B. I. Halpcrin. *Rev. Mod. Phys.* **1977**, *49*, 435.

[50] Y.-F. Zeng, X. Hu, F.-C. Liu, X.-H. Bu. *Chem. Soc. Rev.* **2009**, *38*, 469.

[51] J. M. Zadrozny, D. J. Xiao, M. Atanasov, G. J. Long, F. Grandjean, F. Neese, J. R. Long. *Nat. Chem.* **2013**, *5*, 577.

[52] S. G. Carling, D. Visser, D. Hautot, I. D. Watts, P. Day, J. Ensling, P. Gutlich, G. J. Long, F. Grandjean. *Phys. Rev. B* **2002**, *66*, 104407.

[53] Z.-D. Fu, Y.-Z. Zheng, Y.-G. Xiao, S. Bedanta, A. Senyshyn, G. G. Simeoni, Y.-X. Su, U.

Rücker, P. Kögerler, T. Brückel. *Phys. Rev. B* **2013**, *87*, 214406.

[54] I. A. Blech, B. L. Averbach. *Physics* **1964**, *1*, 31.

[55] Z.-D. Fu, P. Kögerler, U. Rücker, Y.-X. Su, R. Mittal, T. Brückel. *New Journal of Physics* **2010**, *12*, 083044.

[56] M. Gabay, G. Toulouse. *Phys. Rev. Lett.* **1981**, *47*, 201.

[57] W.F. Wolff, J. *Z.* Zittartz. *Phys. B - Condensed Matter* **1985**, *60*, 185.

[58] W. R. Chen, F. C. Zhang, J. Miao, B. Xu, X. L. Dong, L. X. Cao, X. G. Qiu, B. R. Zhao, P.-C. Dai. *Appl. Phys. Lett.* **2005**, *87*, 042508.

[59] B. Henniont, M. Henniont, F. Hippert, A. P. Muranis. *J. Phys. F: Met. Phys.* **1984**, *14*, 489.

[60] J.-K. Jiang, Q.-H. Liang, R.-S. Meng, Q. Yang, C.-J. Tan, X. Suna and X.-P. Chen. *Nanoscale*, **2017**, *9*, 2992.

[61] Y. Zhou, Z. Wang, P. Yang, X. Zu, L. Yang, X. Sun and F. Gao. *ACS Nano*, **2012**, *6*, 9727.

[62] H. Jin, Y. Dai, B. Huang and M. H. Whangbo. *Appl. Phys. Lett.*, **2009**, *94*, 162505.

[63] G. M. Sheldrick, et al. *SADABS 2.05*, University Göttingen, Germany, **2002**.

[64] *SHELXTL 6.10*, Bruker Analytical Instrumentation, Madison, Wisconsin, USA, **2000**.

[65] H. Zentrum. *Journal of large-scale research facilities* **2015**, *1*, A27. http://dx.doi.org/10.17815/jlsrf-1-33.

[66] O. Schärpf, H. Capellmann. *Phys. Status Solidi A*. **1993**, *135*, 359.

[67] F. Neese, et al. ORCA (3.0.2)-An *ab initio*, DFT and semiempirical SCF-MO package, (Max-Planck-Institute for Chemical Energy Conversion, Stiftstr. 34-36, 45470 Mulheim a. d. Ruhr, Germany).

[68]S. E. Stavretis, M. Atanasov, A. A. Podlesnyak, S. C. Hunter, F. Neese, Z.-L. Xue. *Inorg. Chem*. **2015**, *54*, 9790.

[69]F. Weigend, R. Ahlrichs. *Phys. Chem. Chem. Phys*. **2005**, *7*, 3297.

[70]A. Schafer, C. Huber, R. Ahlrichs. *J. Chem. Phys*. **1994**, *100*, 5829.

[71]T. Nakajima, K. Hirao. *Chem. Rev*. **2012**, *112*, 385.

[72]M. Reiher. *Theor. Chem. Acc*. **2006**, *116*, 241.

## Figures

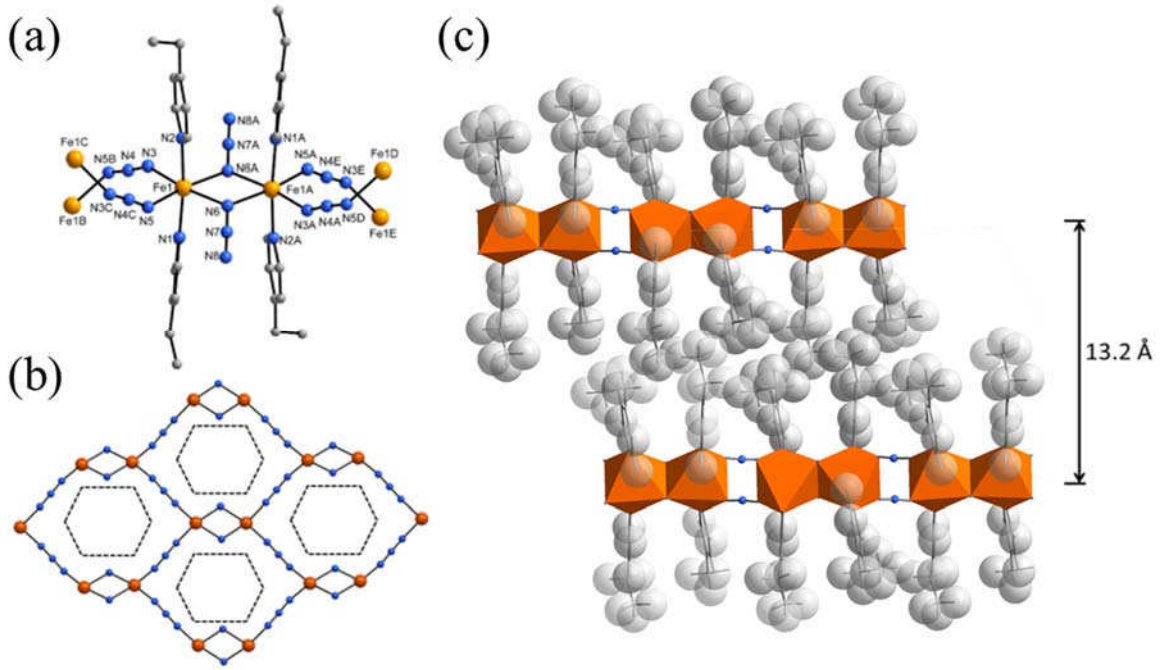


**Figure 1**. The asymmetric unit (a), 2D dimerized honeycomb structure (b) and interlayer-packing view (c) of FEN. The dashed line represents the hexagon of the dimerized honeycomb lattice. Hydrogen atoms are highlighted in van der Waals mode.

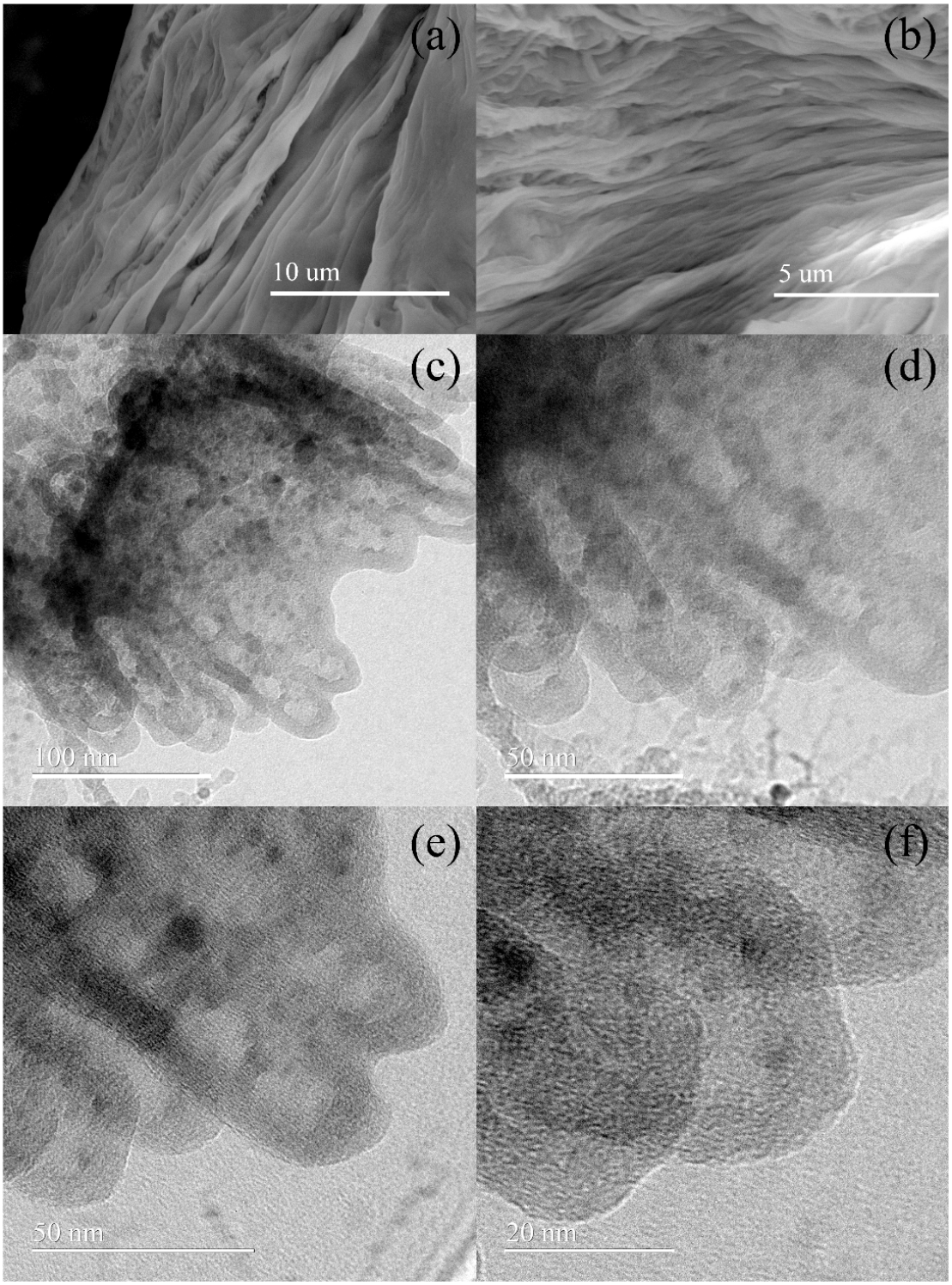


**Figure 2.** SEM images (a, b) of powder FEN sample and TEM images (c-f) taken from the methanol dispersed FEN sample.

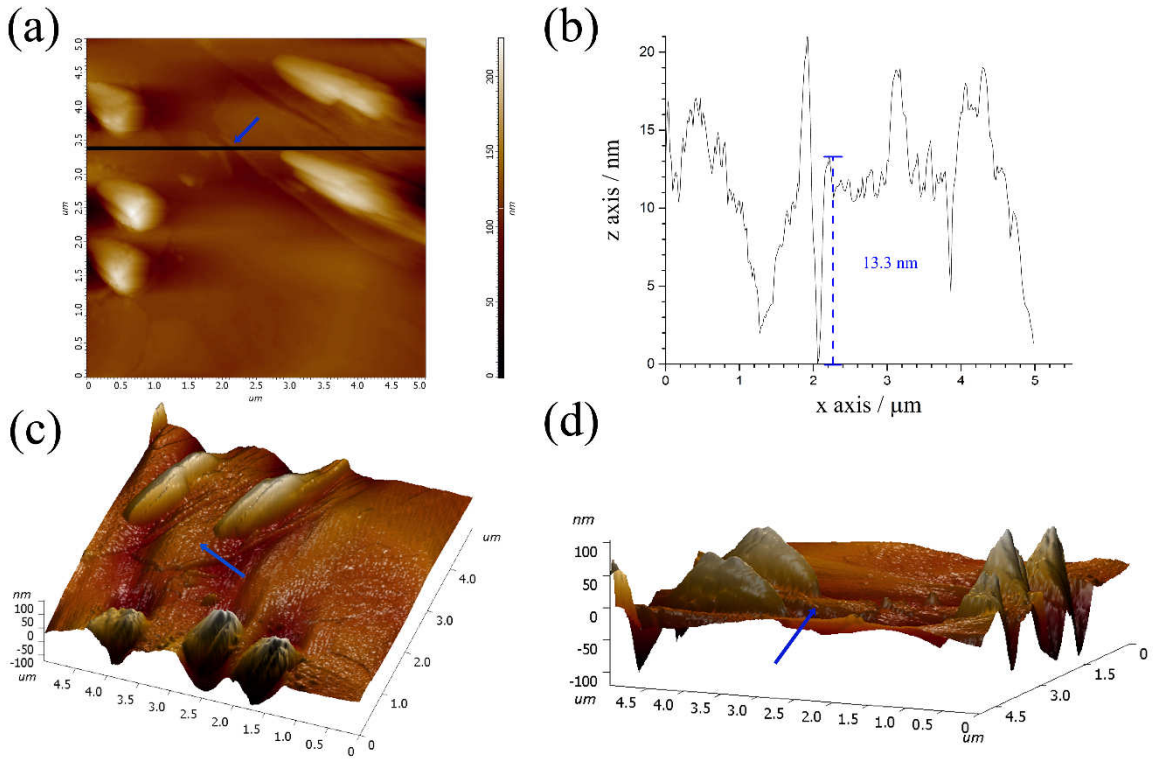


**Figure 3.** 2D AFM height images (a), profile height counting corresponding to the blue arrow (b), topographical AFM image (c) and cross-sectional image (d) for FEN.

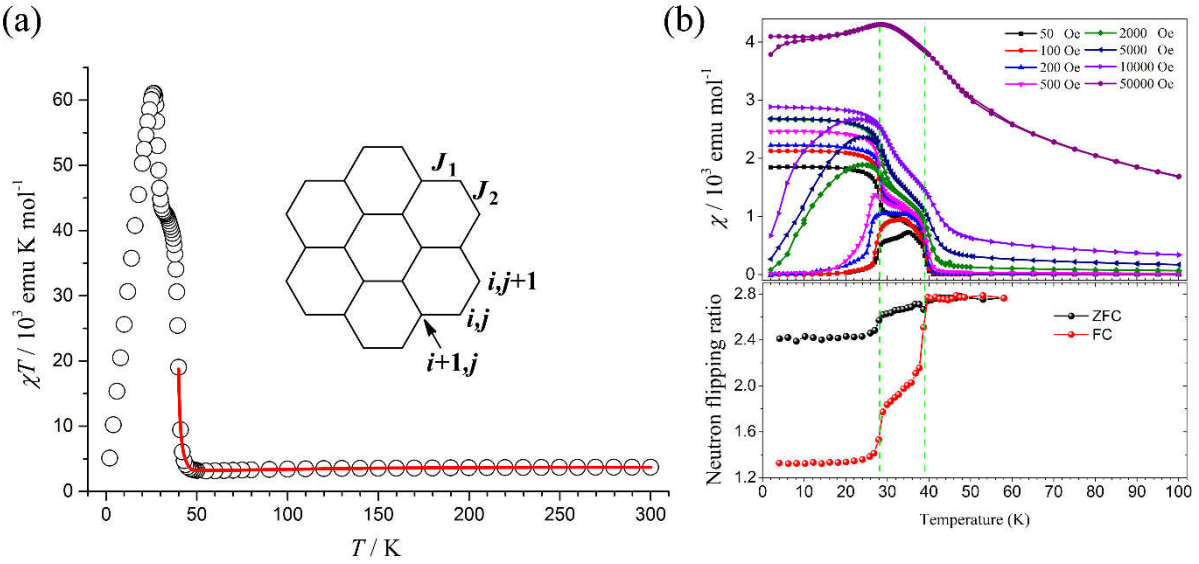


**Figure 4**. (a) Temperature dependence of $\chi T$ obtained at 1000 Oe. The red line corresponds to the best fit with Curély's model. (b) Top: ZFC and FC magnetization versus temperature curves of FEN measured with applied fields of 50-50000 Oe; Bottom: Temperature dependence of the flipping ratios of the neutron spins measured at the (100) Bragg peak after ZFC and FC protocols. The green lines are guides for the eyes.

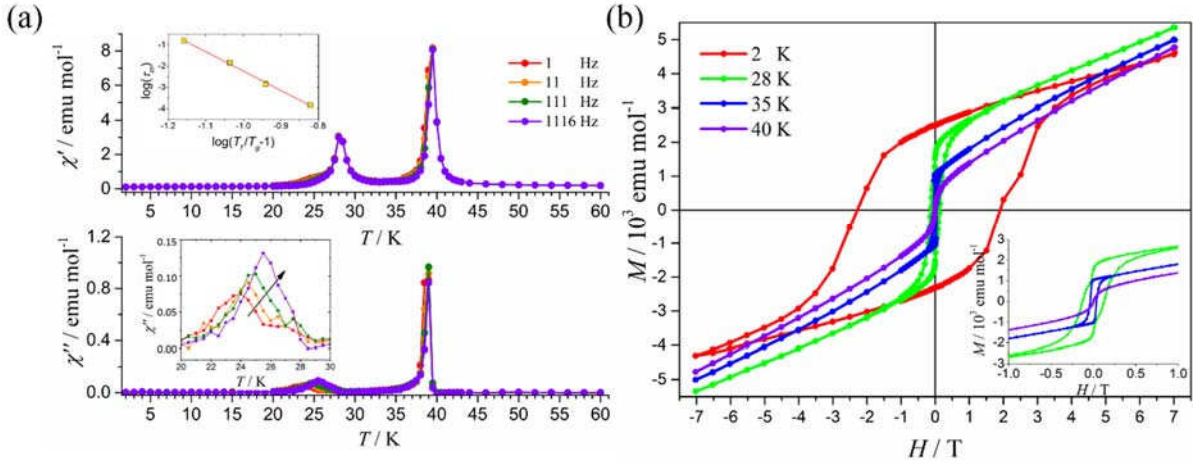


**Figure 5**. (a) Temperature dependence of the in-phase $\chi'$ (top) and out-of-phase $\chi''$ (bottom) ac susceptibility for FEN under zero dc field. Inset of (a) top: the plot of $\log_{10}(\tau_m)$ vs $\log_{10}(T_f/T_g - 1)$. The red line represents the linear fit using Eq. (4). Inset of (a) bottom: enlargement of the $\chi''$ curves in the temperature range from 20 to 30 K. (b) Hysteresis loops of FEN measured at 2-40 K. Insert of (b): The enlarged Hysteresis loops of **1** measured at 28, 35 and 40 K. The lines are guides for the eyes.

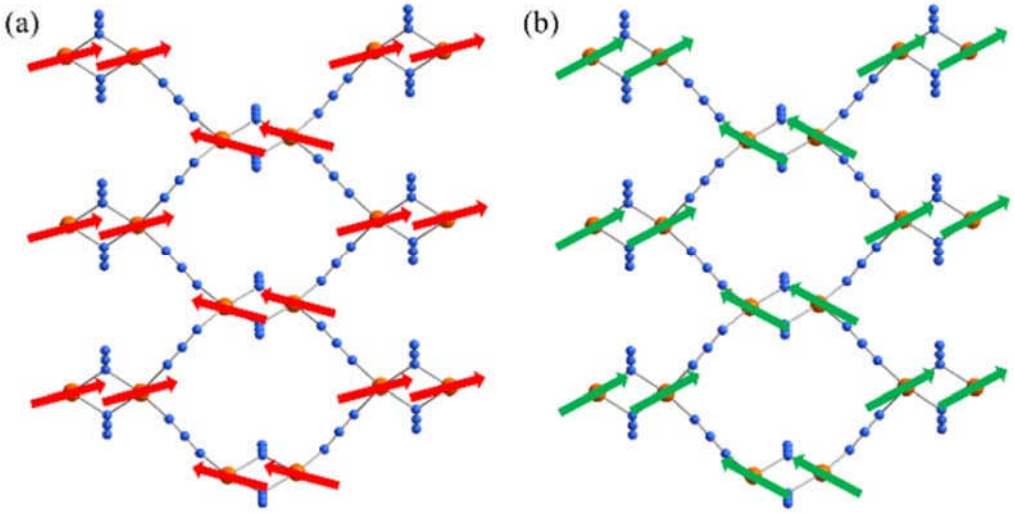


**Figure 6**. Proposed spin configuration of FEN at 39 K (a) and 28 K (b). The arrows represent individual moments of Fe(II) centers.

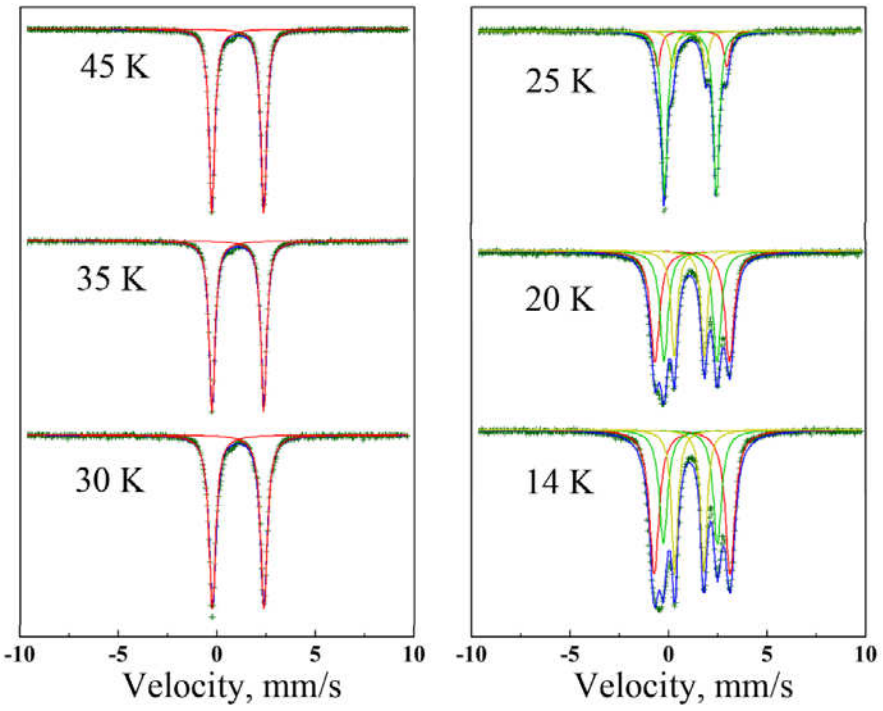

**Figure 7**. The Mössbauer spectra of FEN taken at various temperatures. The solid lines are the best fits of iron(II) ions.

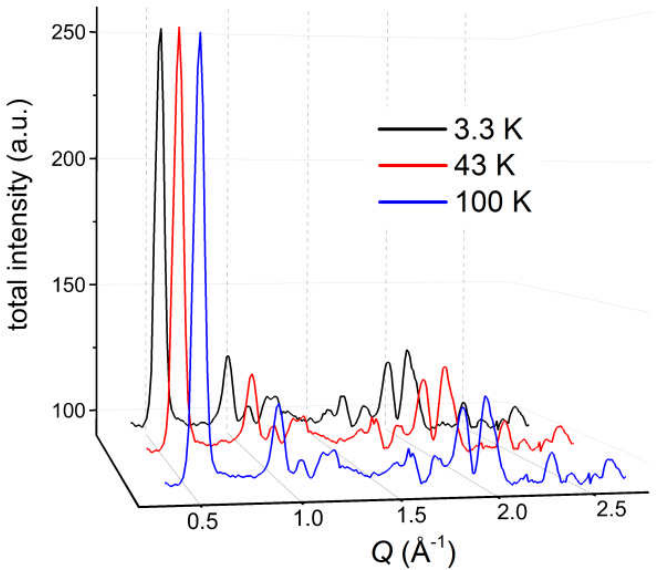


**Figure 8.** Total neutron scattering intensity measured on DNS at 3.3, 43, and 100 K.

The table of contents entry should be 50−60 words long and should be written in the present tense and impersonal style (i.e., avoid we). The text should be different from the abstract text.

A dimerized honeycomb lattice with integer spins is realized in an iron(II)-azido compound. Magnetic, Mössbauer and polarized neutron scattering spectroscopy studies reveal a reentrant spin-glass behavior, which leads to a "very hard" magnetic hysteresis loop at lower temperatures.

**Keyword:** 2D frustrated magnets, dimerized honeycomb lattice, iron(II), spin glass, neutron scattering

Yuan-Qi Zhai, Yi-Fei Deng, Peng-Bo Jin, Zhendong Fu*, Erxi Feng, Yixi Su, Takuya Shiga, Hiroki Oshio, and Yan-Zhen Zheng*

**Reentrant Spin-Glass and Large Coercive Field Observed in the Spin Integer Dimerized Honeycomb Lattice**

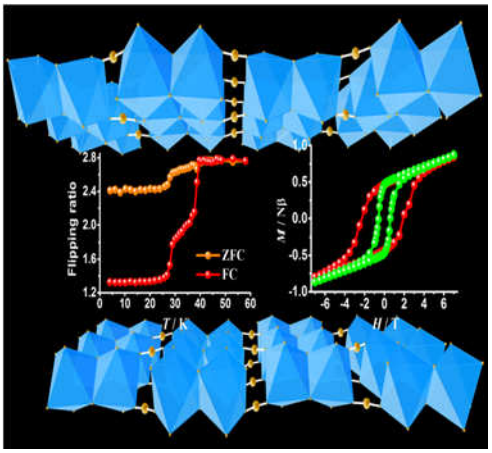


ToC figure ((Please choose one size: 55 mm broad × 50 mm high **or** 110 mm broad × 20 mm high. Please do not use any other dimensions))

# Supporting Information

Reentrant Spin-Glass and Large Coercive Field Observed in the Spin Integer Dimerized Honeycomb Lattice

*Yuan-Qi Zhai, Yi-Fei Deng, Peng-Bo Jin, Zhendong Fu*, Erxi Feng, Yixi Su, Takuya Shiga, Hiroki Oshio, and Yan-Zhen Zheng**

**Table S1.** Crystal data and structure refinement for FEN.

| | 150(2) K | 20(2) K |
|---|---|---|
| Empirical formula | $C_{14}H_{18}FeN_8$ | $C_{14}H_{18}FeN_8$ |
| Formula weight/g mol$^{-1}$ | 354.21 | 354.21 |
| Crystal system | monoclinic | monoclinic |
| Space group | $P2_1/c$ | $P2_1/c$ |
| $a$, Å | 14.335(14) | 13.9565(12) |
| $b$, Å | 8.479(9) | 8.434(3) |
| $c$, Å | 15.526(16) | 15.2198(5) |
| $\alpha$, deg | 90 | 90 |
| $\beta$, deg | 116.501(11) | 116.387(6) |
| $\gamma$, deg | 90 | 90 |
| $V$, Å$^3$ | 1689(3) | 1604.9(6) |
| Z | 4 | 4 |
| $d_{cal}$ / g cm$^{-3}$ | 1.393 | 1.466 |
| $\theta$ range | 1.59–27.86° | 3.79-37.03° |
| Completeness | 98.5% | 70.4% |
| Residual map, e Å$^{-3}$ | 0.306 and –0.359 | 1.333 and –0.932 |
| Goodness-of-fit on $F^2$ | 1.034 | 1.074 |
| Final indices [$I > 2\sigma(I)$] | $R_1 = 0.0347$, $wR_2 = 0.0879$ | $R_1 = 0.0739$, $wR_2 = 0.2321$ |
| $R$ indices (all data) | $R_1 = 0.0555$, $wR_2 = 0.0979$ | $R_1 = 0.0777$, $wR_2 = 0.2364$ |

**Table S2.** Selected bond lengths (Å) and angles (deg) for FEN.

| | 150(2) K | 20(2) K |
|---|---|---|
| Fe(1)-N(1) | 2.217(2) | 2.205(5) |
| Fe(1)-N(2) | 2.212(2) | 2.202(5) |
| Fe(1)-N(3) | 2.160(2) | 2.132(7) |
| Fe(1)-N(5) | 2.158(2) | 2.138(5) |
| Fe(1)-N(6) | 2.237(2) | 2.195(5) |
| Fe(1)-N(6A) | 2.199(2) | 2.188(4) |
| N(1)-Fe(1)-N(2) | 174.32(6) | 174.07(14) |
| N(1)-Fe(1)-N(3) | 88.48(10) | 89.5(2) |
| N(1)-Fe(1)-N(5) | 88.35(9) | 87.1(2) |
| N(1)-Fe(1)-N(6) | 92.50(9) | 92.23(16) |
| N(1)-Fe(1)-N(6a) | 93.41(8) | 92.33(16) |
| N(2)-Fe(1)-N(3) | 89.20(10) | 88.3(2) |
| N(2)-Fe(1)-N(5) | 86.95(9) | 87.9(2) |
| N(2)-Fe(1)-N(6) | 90.73(9) | 90.99(16) |
| N(2)-Fe(1)-N(6A) | 91.85(8) | 93.20(16) |
| N(3)-Fe(1)-N(5) | 99.86(12) | 101.0(2) |
| N(3)-Fe(1)-N(6) | 169.45(8) | 168.41(18) |
| N(3)-Fe(1)-N(6A) | 92.05(10) | 90.34(18) |
| N(5)-Fe(1)-N(6) | 90.67(11) | 90.54(18) |
| N(5)-Fe(1)-N(6A) | 168.01(8) | 168.63(18) |
| N(6)-Fe(1)-N(6A) | 77.41(10) | 78.13(19) |
| Fe(1)- N(6)-Fe(1A) | 102.59(10) | 101.87(19) |

Symmetry transformations used to generate equivalent atoms: A –x, –y+1, –z; B -x, y-1/2, -z+1/2; C -x, y+1/2, -z+1/2

**Table S3.** Mossbauer spectral parameters of FEN in the temperature 14 – 45 K.

| $T$ / K | $\delta_1$ / mm/s | $\delta_2$ / mm/s | $\delta_3$ / mm/s | $E_{Q1}$ / mm/s | $E_{Q2}$ / mm/s | $E_{Q3}$ / mm/s | Area$_1$ | Area$_2$ | Area$_3$ |
|---|---|---|---|---|---|---|---|---|---|
| 45K | 1.198 | | | 2.695 | | | | | |
| 35K | 1.198 | | | 2.681 | | | | | |
| 30K | 1.199 | | | 2.682 | | | | | |
| 25K | 1.290 | 1.199 | 1.132 | 3.580 | 2.692 | 1.720 | 0.156 | 0.697 | 0.147 |
| 20K | 1.302 | 1.200 | 1.128 | 3.607 | 2.689 | 1.678 | 0.217 | 0.609 | 0.174 |
| 14K | 1.296 | 1.196 | 1.137 | 3.914 | 2.782 | 1.502 | 0.425 | 0.294 | 0.281 |

**Supporting Figures**

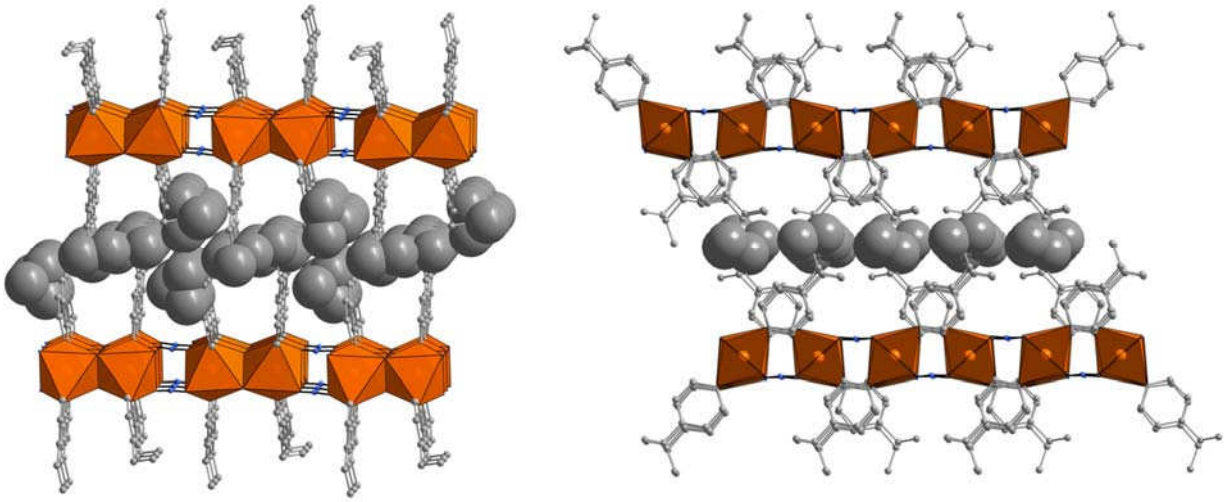

**Figure S1**. The packing diagrams of FEN. Hydrogen atoms at the interface of two layers are highlighted in van der Waals mode.

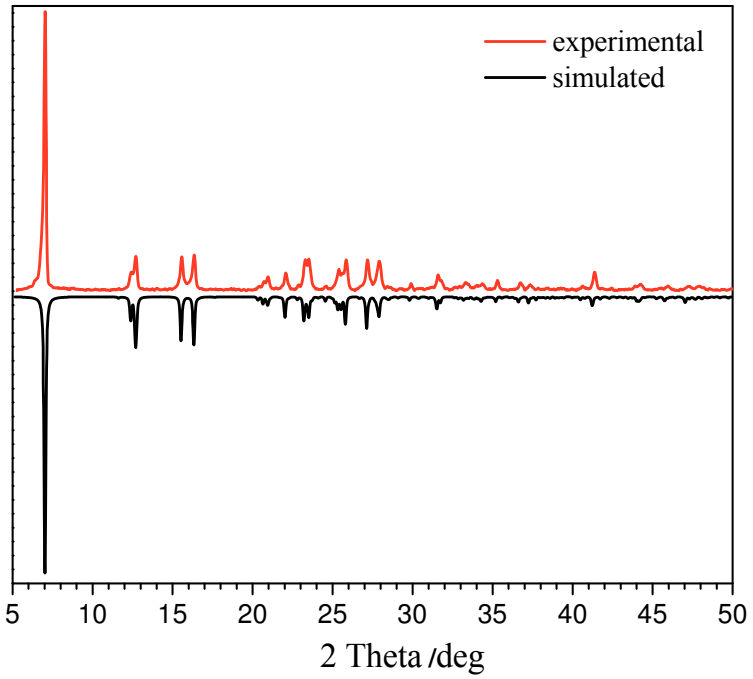


**Figure S2**. The experimental and calculated powder XRD patterns of FEN.

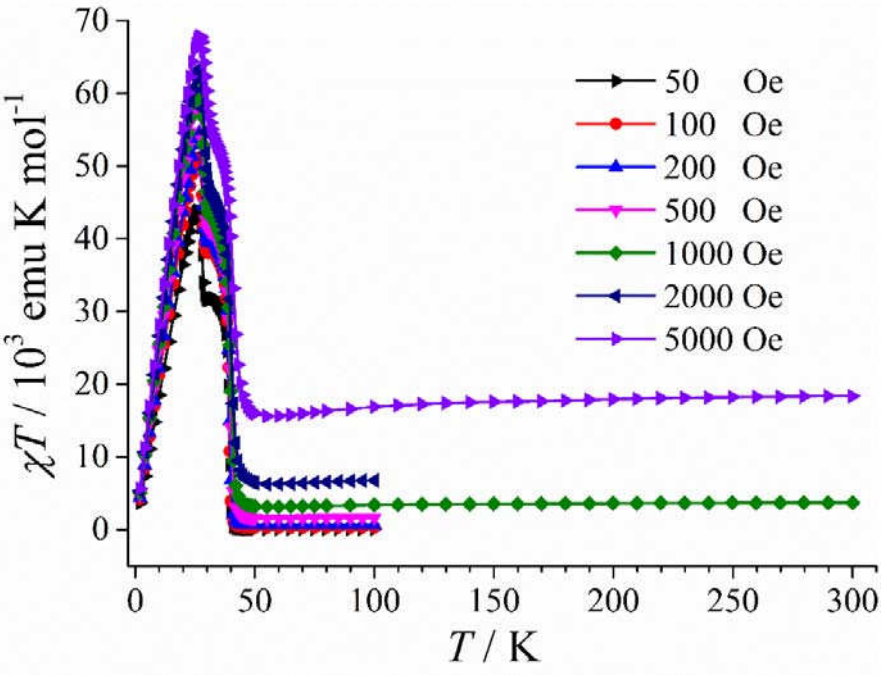


**Figure S3**. $\chi T$ versus $T$ plots for FEN under different dc fields. The lines are guides to the eyes.

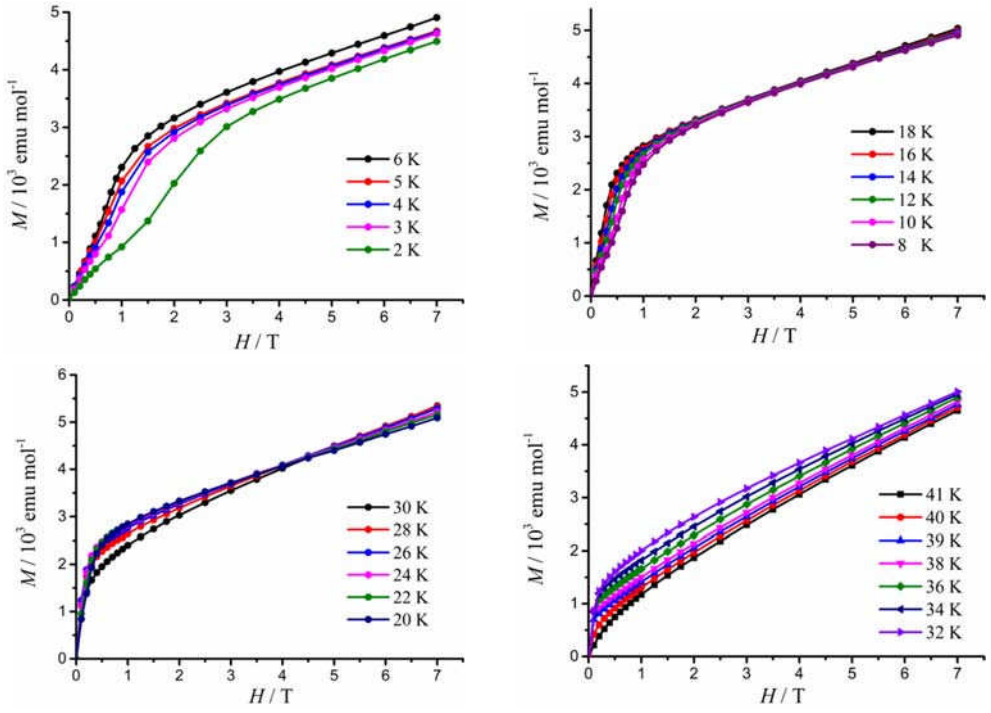


**Figure S4.** Field dependence of the magnetization at 2-41 K for FEN. The lines are guides for the eyes.

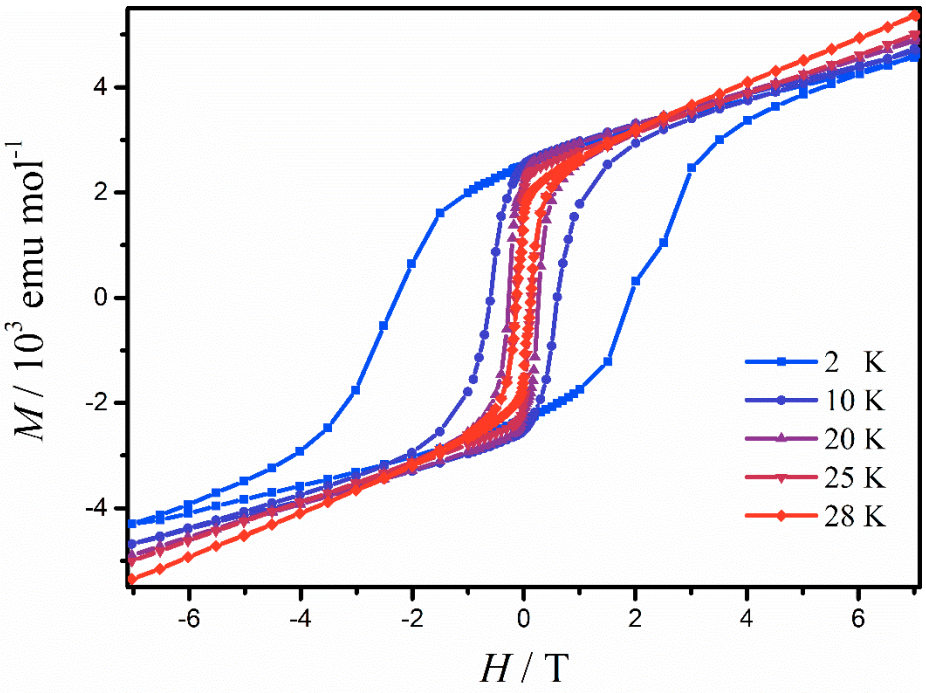


**Figure S5**. Hysteresis loops of FEN measured at 2-28 K. The lines are guides for the eyes.

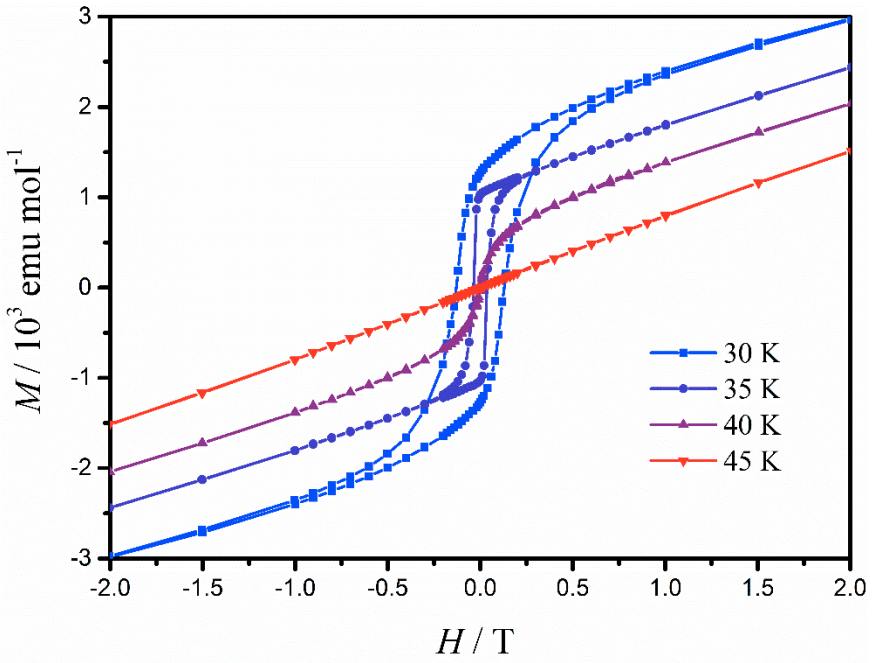

**Figure S6**. Hysteresis loops of FEN measured at 30-45 K. The lines are guides for the eyes.

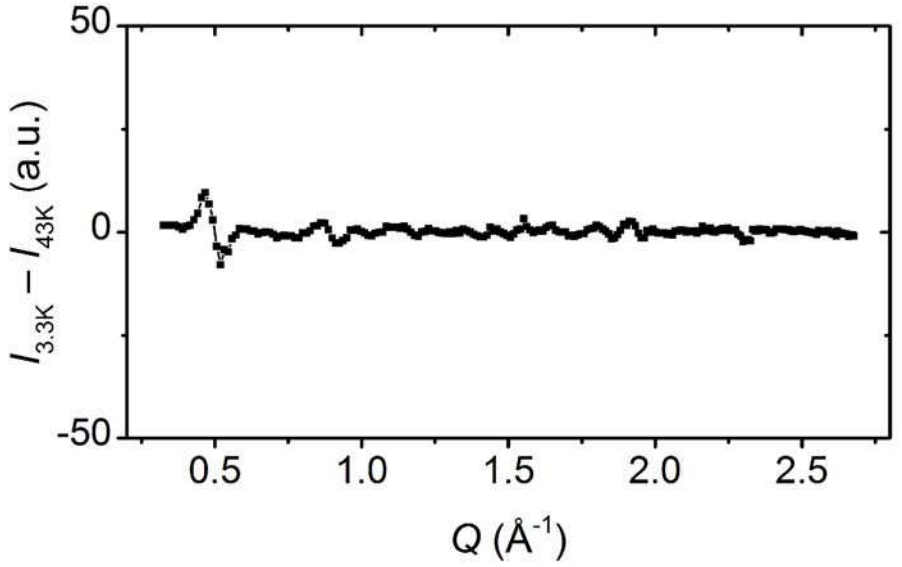


**Figure S7**. The difference pattern obtained by subtracting the scattering intensity for 43 K from the one for 3.3 K.

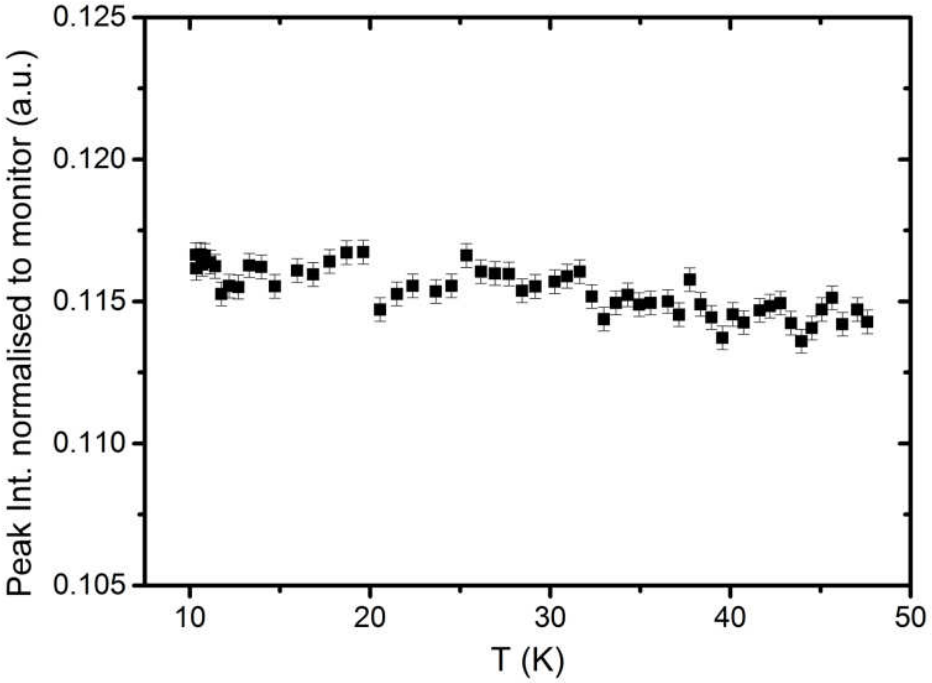

**Figure S8**. Temperature dependence of the peak intensity of (110) reflection.

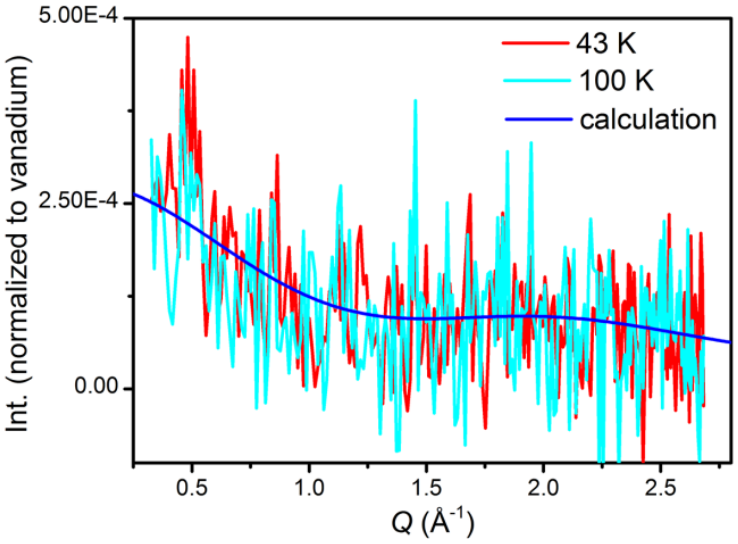


**Figure S9**. Magnetic scattering intensities measured at 43 (red) and 100 (cyan) K. The calculated spin correlation of the ferromagnetic $Fe^{2+}$ dimers in FEN is shown as the blue line.

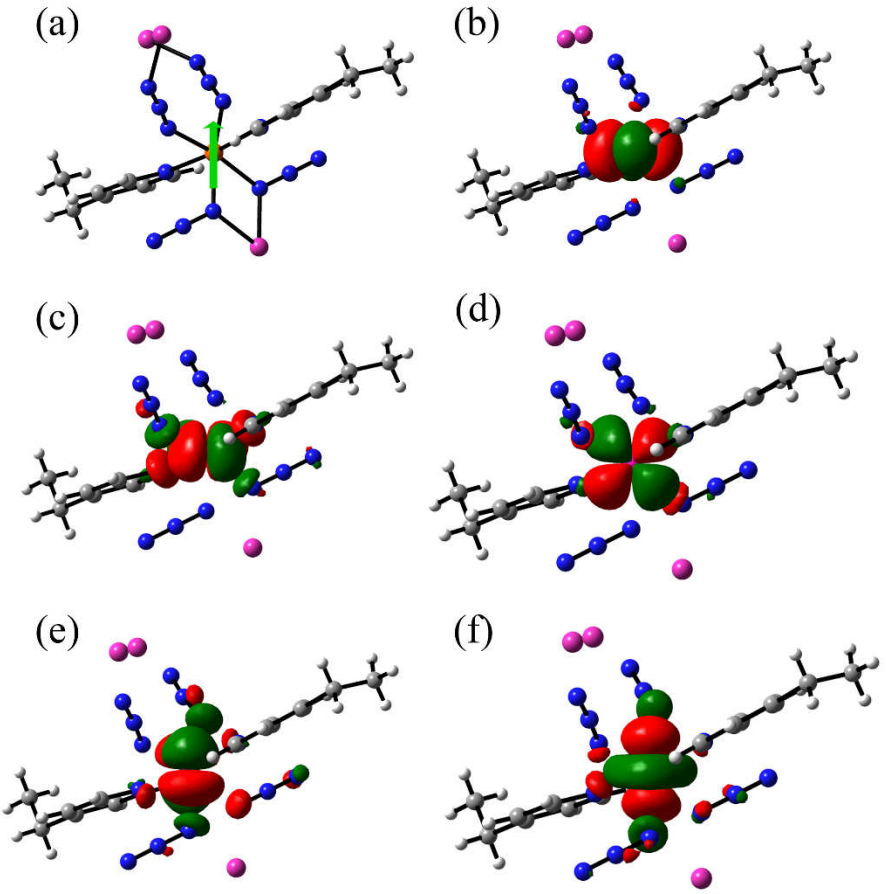


**Figure S10.** (a) Calculated electronic structure of the fragment in FEN (green arrow represent the direction of magnetic moment on the ground state). Colour codes: Fe, orange; N, blue; Zn, pink; C, grey; H: white. (b) – (f) The perspective views of the calculated 3d-orbitals for the quintet ($S = 2$) spin ground state for (b) $d_{x2-y2}$; (c) $d_{xy}$; (d) $d_{yz}$; (e) $d_{xz}$; (f) $d_{z2}$.

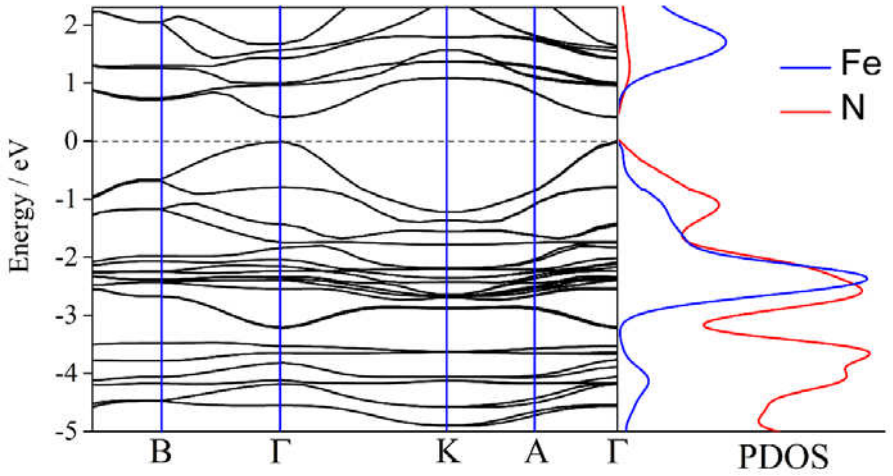


**Figure S11.** Calculated energy band structures (left) and projected density of states (PDOS) (right) for FEN.